






## Magnetic-Field-Compatible Superconducting Transmon Qubit

A. Kringhøj <sup>1,2,†</sup> T. W. Larsen,<sup>1,2,†</sup> O. Erlandsson,<sup>1,2</sup> W. Uilhoorn <sup>3</sup> J.G. Kroll <sup>3</sup> M. Hesselberg,<sup>1,2</sup> R.P.G. McNeil <sup>1,2</sup> P. Krogstrup,<sup>1,4</sup> L. Casparis,<sup>1,2</sup> C.M. Marcus,<sup>1,2</sup> and K.D. Petersson <sup>1,2,\*</sup>

<sup>1</sup>Center for Quantum Devices, Niels Bohr Institute, University of Copenhagen, Copenhagen 2100, Denmark

<sup>2</sup>Microsoft Quantum Lab—Copenhagen, Niels Bohr Institute, University of Copenhagen, Copenhagen 2100, Denmark

<sup>3</sup>QuTech and Kavli Institute of Nanoscience, Delft University of Technology, GA Delft 2600, The Netherlands

<sup>4</sup>Microsoft Quantum Materials Lab—Copenhagen, Lyngby 2800, Denmark



(Received 12 January 2021; revised 18 March 2021; accepted 23 March 2021; published 3 May 2021)

We present a hybrid semiconductor-based superconducting qubit device that remains coherent at magnetic fields up to 1 T. The qubit transition frequency exhibits periodic oscillations with the magnetic field, consistent with interference effects due to the magnetic flux threading the cross section of the proximitized semiconductor nanowire junction. As the induced superconductivity revives, additional coherent modes emerge at high magnetic fields, which we attribute to the interaction of the qubit and low-energy Andreev states.

DOI: [10.1103/PhysRevApplied.15.054001](https://doi.org/10.1103/PhysRevApplied.15.054001)

### I. INTRODUCTION

Superconductor-semiconductor-superconductor (S-Sm-S) nanowire Josephson junctions have been integrated into various superconducting circuits, including gate-voltage-tunable transmon qubits, known as gatemons [1,2], tunable superconducting resonators [3], and Andreev qubits [4,5]. These hybrid junction elements allow *in situ* voltage control of their Andreev spectra and current-phase relation [6–9], in turn influencing measurable qubit properties such as anharmonicity [10] and charge dispersion [11,12]. Moreover, S-Sm nanowires in the presence of strong magnetic fields may host Majorana zero modes—as evidenced by both dc-tunneling and Coulomb-blockade-spectroscopy measurements [13,14]—potentially forming the basis of robust topological qubits [15].

Recent work has demonstrated the coherent operation of gatemons with S-Sm-S nanowire junctions at moderate magnetic fields of approximately 100 mT [16–18]. Spectroscopy of S-Sm-S nanowire fluxonium qubits [19] and graphene-based gatemons [20] at high magnetic fields (approximately 1 T) has also been shown. However, the detailed spectrum and the time-domain coherence properties of gatemons at large magnetic fields remain unexplored. The realization of a magnetic-field-compatible transmon qubit would open up a number of possible new research directions. For instance, a direct Josephson coupling of Majorana zero modes on separate topological

superconductors is expected to modify the energy spectrum of a transmon qubit [21,22], offering a potential route to time-domain studies of topological systems. Studies of other subgap features such as Andreev bound states [5,23] could also take advantage of similar magnetic-field-compatible microwave circuitry. Furthermore, transmon qubits that can operate in high magnetic fields might enable control of a variety of spin-ensemble-based quantum memories [24,25] or allow the origin of  $1/f$  flux noise to be further elucidated through studying the polarization of spin impurities [16,26,27].

In this work, we present a high-magnetic-field-resilient nanowire-based transmon circuit. We demonstrate coherent qubit operation for in-plane magnetic fields up to 1 T. Further, we observe a field-dependent periodic lobe structure in the qubit spectrum, attributable to interference effects as an integer number of flux quanta thread the nanowire cross section. Finally, we observe a rich spectrum of additional energy excitations as we transition into the first and second lobes of the qubit spectrum. We associate these excitations with Andreev states, visible due to their coupling to the qubit.

### II. MAGNETIC-FIELD-COMPATIBLE GATEMON DEVICE

Figure 1 shows the qubit device. A 20-nm-thick Nb-Ti-N film on a high-resistivity silicon substrate is patterned by electron-beam lithography and a chlorine-based dry-etch process to form the  $\lambda/2$  readout resonator, qubit island, and bottom-gate electrodes [see Fig. 1(a)]. We additionally pattern a high density of flux-pinning holes,

\*karl.petersson@microsoft.com

†These authors contributed equally.

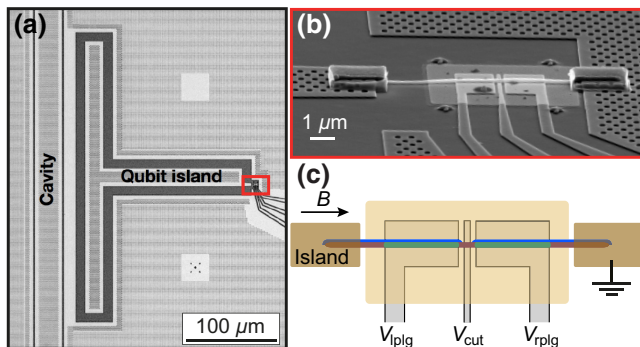


FIG. 1. The magnetic-field-compatible device. (a) A micrograph of the transmon qubit island capacitively coupled to a  $\lambda/2$  cavity for readout and microwave control. The ground planes and inner conductors of the island and resonator are patterned with a large density of flux-pinning holes for compatibility with large magnetic fields. A nanowire is placed to the right of the island (red rectangle). (b) A scanning electron micrograph of the nanowire and the bottom gates. One side of the wire junction is connected to the island and the other side is connected to the ground plane. (c) A schematic of the device, showing an InAs nanowire (brown) with one side covered in aluminum (blue) placed on top of two plunger gates ( $V_{lplg}$  and  $V_{rplg}$ ) that tune the chemical potential in sections (green) of the proximitized InAs. A small region of the superconductor between these two segments is removed to create a Josephson junction, controlled by  $V_{cut}$ . A magnetic field,  $B$ , is applied along the wire axis.

allowing high-field compatibility of the qubit capacitor and readout resonator [20,28]. Nb-Ti-N crossovers short ground planes together to prevent parasitic chip modes [29].

A nanowire is placed on the Nb-Ti-N bottom gates using a micromanipulator. The nanowire has an InAs core, with a diameter of approximately 100 nm, two out of six facets being covered by a 7-nm-thick epitaxially matched aluminum film [30]. Prior to the initial Nb-Ti-N deposition, a local region of 5 nm thick  $\text{HfO}_2$  is deposited using atomic-layer-deposition techniques to ensure no leakage between the closely spaced gates through the silicon substrate [31]. A second thicker  $\text{HfO}_2$  layer (15 nm) is deposited on top of the bottom gates as a gate dielectric. To form the Josephson junction, a small segment of the aluminum shell (approximately 100 nm) is removed by wet etching [2].

To complete the gatemon qubit circuit, the nanowire is connected to the T-shaped qubit island, with simulated charging energy  $E_C/h = 230$  MHz [32], and to the surrounding ground plane [see Fig. 1(b)]. A light rf mill is used to remove the native oxide of InAs prior to depositing approximately 200-nm Nb-Ti-N sputtered contacts. The qubit island is capacitively coupled to the  $\lambda/2$  cavity with resonance frequency  $f_r \sim 4.95$  GHz for readout and microwave control. Large plunger electrodes,  $V_{lplg}$  and  $V_{rplg}$ , allow for tuning of the chemical potential of the two proximitized nanowire segments on each side of

the Josephson junction [green segments of Fig. 1(c)]. A third electrode,  $V_{cut}$ , located under the junction, tunes the Josephson energy,  $E_J$ , and in turn the qubit frequency,  $f_q$ . On-chip LC-filters (not shown) on each gate electrode suppress microwave dissipation through the capacitively coupled gates [33]. A second qubit with no plunger gates is coupled to the same resonator (not shown).

We present data from the qubit device shown in Fig. 1, which maintains coherence up to magnetic fields of 1 T. For multiple similar devices, we observe coherent operation up to approximately 500 mT. The sample is placed inside a Cu-Be enclosure filled with microwave-absorbing Eccosorb foam to reduce stray microwave and infrared radiation. The enclosure is mounted inside a bottom-loading dilution refrigerator equipped with a 6-1-1 T three-axis vector magnet and with a base temperature  $< 50$  mK (for further details, including a schematic of the setup, see Appendix B).

### III. QUBIT MEASUREMENTS IN LARGE MAGNETIC FIELDS

We investigate the qubit behavior by performing two-tone spectroscopy as a function of the magnetic field,  $B$ , aligned along the nanowire axis. A varying drive tone at frequency  $f_d$  is applied, followed by a readout tone for each  $B$ . During these measurements, the cavity resonance is first measured for each  $B$  in order to correct for any changes in the readout frequency. Out-of-plane magnetic fields on the order of 10  $\mu\text{T}$  modify the resonance frequency of the cavity; however, we do not observe any degradation in the resonator  $Q$  factor as the total magnetic field is varied. While changing  $B$ , intermittent corrections to the magnetic field alignment are also applied to minimize the out-of-plane magnetic field component (for details, see Appendix A).

Figure 2 shows the qubit spectrum as a function of  $B$  up to 1 T. The qubit spectrum exhibits a lobe structure, with three lobes separated by minima at  $B \sim 0.225$  T and  $B \sim 0.675$  T and a reduced maximum qubit frequency in higher lobes. These minima may occur due to a suppression of the induced superconducting gap,  $\Delta^*$ , in the leads of the junction due to interference effects [34]. Depending on gate voltage, the charge density in the semiconductor nanowire leads may be confined to the surface (see Fig. 2, inset). As analyzed by Winkler *et al.* [35], a segment of this cross-section geometry effectively forms a superconducting ring interrupted by a semiconductor Josephson junction, with the superconducting gap modulated by the periodic flux-biased phase difference (Fig. 2, inset). For the case of half a flux quantum threading the nanowire at  $B = 0.225$  T, the applied flux  $\Phi$  in units of flux quanta  $\Phi_0$  is shown along the top horizontal axis of Fig. 2. From this period, we estimate the effective diameter of the interference loop to be  $d_{\text{eff}} =$

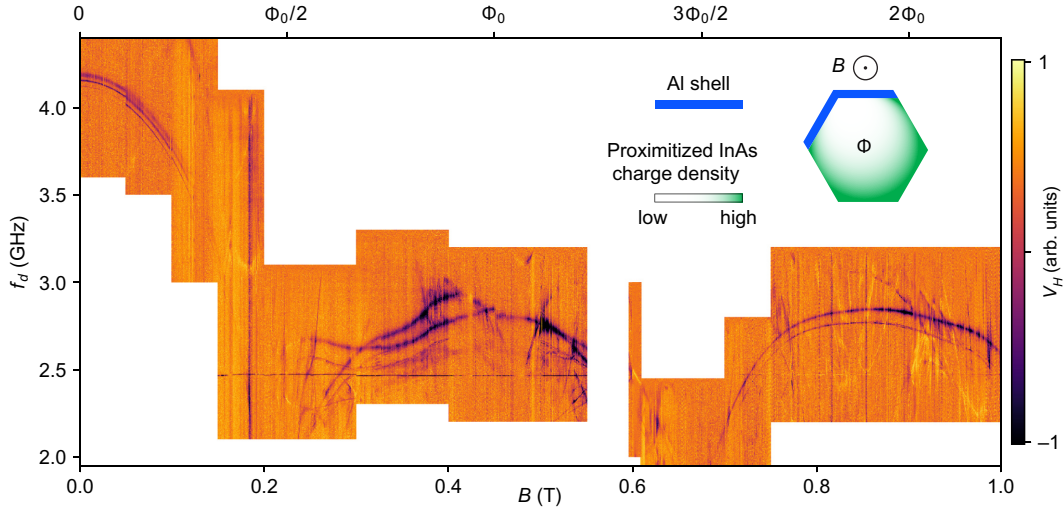


FIG. 2. Two-tone spectroscopy as a function of the magnetic field  $B$  at  $V_{\text{cut}} = -0.5$  V and  $V_{\text{plg}} = V_{\text{rplg}} = -4.2$  V. A variable drive tone,  $f_d$ , is applied and immediately followed by a readout tone at the cavity resonance frequency, allowing readout of the demodulated transmission voltage,  $V_H$ . The qubit drive power is adjusted between traces to account for varying lifetime and detuning from the readout cavity, which may cause changes in the background signal and line widths of transitions. Data around 0.58 T are omitted due to the applied signal power being too low during the two-tone spectroscopy. A line average is subtracted from the data for each  $B$ . The inset is a sketch illustrating the cross section of a two-facet nanowire, with the hypothesis that the electron density accumulates at the InAs surface, as illustrated by the color gradient (green to white). A superconducting ring is created by the superconducting Al shell (blue) and the proximitized InAs (green). For an axial magnetic field,  $B$ , a flux,  $\Phi$ , threads the nanowire cross section, resulting in a periodic modulation of the qubit frequency. The top horizontal axis is constructed by inferring that a half-integer number of flux quanta,  $\Phi_0 (= h/2e)$ , thread the nanowire at  $B = 225$  mT.

$\sqrt{2\Phi_0/\pi B} (\Phi = \Phi_0/2) = 76$  nm. As the charge accumulation layer will have a finite thickness, one expects a slightly smaller effective diameter compared to that of the nanowire (approximately 100 nm) [36]. Simulations of realistic wire geometries [35] also predict a reduced maximum superconducting gap in higher lobes due to inhomogeneity in the effective diameter. This is consistent with our measured data, where the qubit frequency,  $f_q$ , is expected to scale with  $\sqrt{\Delta^*}$ . Similar oscillations with a magnetic field have also been observed for nanowires in transport experiments [37] and have been attributed to interference effects in the junction itself, which may also play a significant role here. We note that the field dependence is strongly influenced by the nanowire charge distribution and the oscillations observed here are for a particular range of plunger-gate values [35,38]. Periodic oscillations in qubit frequency have also been observed for gatemon with nanowire junctions where the Al shell has fully enclosed the leads and have been interpreted as the Little-Parks effect [17,18].

We next consider the qubit behavior in each of the three lobes. In the zeroth lobe measured from  $B \sim 0$  to approximately 150 mT, the qubit behaves indistinguishably from a standard gatemon device. Due to the high drive power, multiphoton transitions are observed, exciting higher-energy states of the qubit. At around 150 mT, the system becomes unmeasurable due to the second qubit on the chip anticrossing with the readout resonator (see

Fig. 5). Figures 3(a) and 3(b) show Rabi oscillations and lifetime decay at  $B = 0$  and  $B = 50$  mT. At  $B = 0$ , we observe lifetimes of approximately  $5.5 \mu\text{s}$ , similar to previous gatemon devices with a single junction gate, indicating that the additional plunger gates and dielectric layers do not compromise the qubit performance. The measurements show almost no difference between  $B = 0$  and  $B = 50$  mT, demonstrating excellent resilience to parallel magnetic fields, consistent with other recent studies of gatemon qubits [16]. Furthermore, as the field is not perfectly aligned, these data indicate that small out-of-plane magnetic fields (approximately  $10 \mu\text{T}$ ) do not degrade the qubit quality. This suggests that our qubit design mitigates the need for extensive magnetic shielding, as typically required for superconducting qubit devices.

Moving to the first lobe between  $B \sim 250$  mT and  $B \sim 650$  mT, two main resonances appear (Fig. 2). Both states behave as weakly anharmonic oscillator modes with a broad single-photon transition frequency and a sharper two-photon transition separated by approximately 100 MHz. While the presence of two anharmonic states is consistent with a large Majorana coupling across the junction mediated by two overlapping zero modes [21], it is unlikely that the splitting is due to Majorana physics as the topological phase is typically expected to occur at higher magnetic fields for InAs-based wires. Rather, the splitting might be connected to low-energy Andreev states

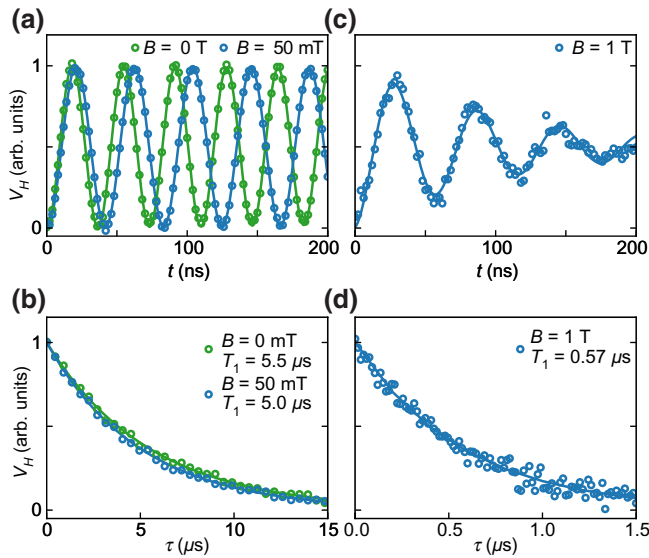


FIG. 3. Time-domain measurements as a function of  $B$  at  $V_{\text{cut}} = -0.5$  V and  $V_{\text{plg}} = V_{\text{rplg}} = -4.2$  V. (a) Rabi oscillations of the gatemon at  $B = 0$  and  $B = 50$  mT. We measure the demodulated transmission,  $V_H$ , as a function of drive duration,  $t$ , applied at the qubit frequency. The fits are exponentially damped sinusoids. The data are normalized to the extracted fit parameters. (b) The  $T_1$ -lifetime measurement at  $B = 0$  and  $B = 50$  mT. We measure  $V_H$  as a function of the delay time,  $\tau$ , between the drive and readout tones. To excite the qubit, we apply a  $\pi$  pulse calibrated from (a) at  $f_q = 4.2$  GHz (green) and  $f_q = 4.1$  GHz (blue). The data are fitted to a decaying exponent to extract  $T_1$ . (c) [(d)] The same as (a) [(b)] at  $B = 1$  T with  $f_q = 2.4$  GHz.

interacting with the qubit mode, as indicated by several transitions dispersing strongly with magnetic field throughout the first lobe. In this regime, it is not possible to probe the qubit states using time-domain measurements due to very low lifetimes.

In the second lobe above  $B \sim 650$  mT, a single qubit resonance revives and is clearly visible all the way up to  $B = 1$  T. The two-photon  $0 \rightarrow 2$  transition is also observed below the qubit transition. Similar to the first lobe, additional resonances strongly dispersing in magnetic field are also observed in the second lobe. In contrast to the first lobe, the qubit is coherently resolved in time-domain measurements throughout the second lobe. Figures 3(c) and 3(d) show coherent Rabi oscillations of a superconducting transmon qubit at  $B = 1$  T with lifetime  $T_1 = 0.57 \mu\text{s}$ . While we do not attempt to measure Ramsey oscillations at  $B = 1$  T, we estimate a pure dephasing time  $T_\phi$  from  $1/T_R = 3/(4T_1) + 1/(2T_\phi)$  [39,40], where  $T_R$  is the Rabi decay time. From the fit in Fig. 3(c), we extract  $T_R = 110$  ns and taking  $T_1 = 0.57 \mu\text{s}$ , we estimate  $T_\phi \sim 60$  ns at  $B = 1$  T. In contrast to a Ramsey measurement that probes the noise spectrum around zero frequency, this dephasing time reflects the noise spectrum at the Rabi frequency,  $\omega_R/2\pi \sim 17$  MHz [40]. At  $B = 0$ , we estimate  $T_\phi \gg 200$

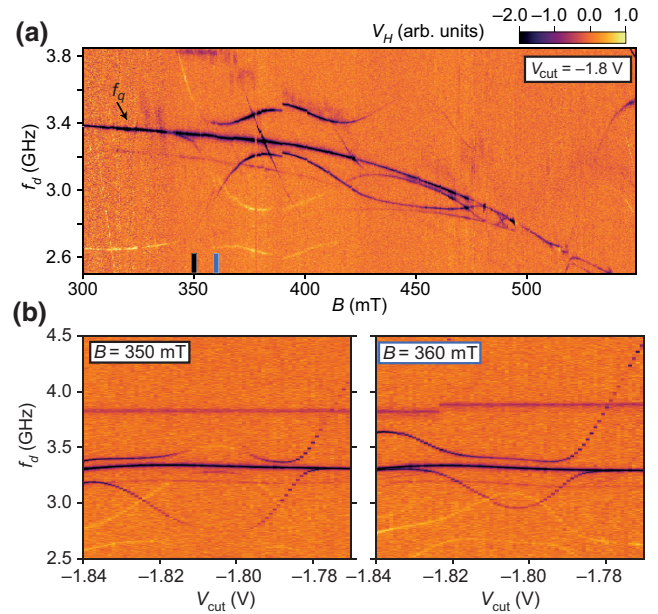


FIG. 4. The junction states as a function of the magnetic field and gate. (a) Two-tone spectroscopy for varying  $f_d$  and  $B$  reveals the oscillating behavior of the junction states at gate voltages  $V_{\text{cut}} = -1.8$  V and  $V_{\text{plg}} = V_{\text{rplg}} = -2.0$  V. We observe an uninterrupted qubit transition frequency  $f_q$  (arrow) decaying as  $B$  increases with multiple new transitions emerging and exhibiting multiple avoided crossings with the qubit transition. (b) Two-tone spectroscopy as a function of  $f_d$  and  $V_{\text{cut}}$  at  $B = 350$  mT [left, black rectangle in (a)] and  $360$  mT [right, blue rectangle in (a)]. Again, a clear qubit transition is visible, weakly dependent on  $V_{\text{cut}}$  with two strongly dispersing transitions coupling to the qubit. The gate-independent transition at  $f_d \sim 3.8$  GHz is the qubit transition of the second qubit. A line average is subtracted from each column in all panels.

ns as both  $T_1$  and  $T_R$  are much longer than the 200-ns measurement window.

Comparing with previous work, we attribute the enhanced magnetic field resilience to the use of thin-shell nanowires (approximately 7 nm) as opposed to the thicker Al shells (approximately 30-40 nm) used in Refs. [16–18]. Another key difference is the use of nanowires where not all facets are covered with Al, allowing voltage control of the charge density in the proximitized semiconductor leads. We speculate that the differences in  $T_1$  times between the three lobes is the result of a varying density of subgap states [18]. While not presently under full experimental control, this difference is likely specific to the charge distribution in the wire for a given device tuning. In addition, we speculate that the decrease in  $T_1$  at  $B = 1$  T compared to at  $B = 0$  is also influenced by the reduction in  $\Delta^*$ , resulting in an increase in quasiparticle poisoning rates [41,42].

#### IV. ANOMALOUS JUNCTION STATES

To investigate the anomalous qubit-resonance splittings in the first lobe, we focus on a voltage regime where sharp additional transitions and avoided crossings in the qubit transition are observed, as shown in Fig. 4(a). A clear uninterrupted qubit transition frequency  $f_q$  is slowly reduced from  $f_q \sim 3.4$  to 2.8 GHz, as  $B$  is increased from 300 to 500 mT [arrow in Fig. 4(a)]. Additionally, around the qubit transition, several new resonances appear for  $B > 350$  mT, oscillating with magnetic field. When these oscillating state transitions are on resonance with the qubit, we observe avoided crossings, indicating strong coupling to the qubit. We associate these resonances with low-energy Andreev bound states that couple to the resonator via the qubit, in agreement with recent numerical simulations of similar nanowire structures [43]. We speculate that the coexistence of the coupled and uncoupled spectra, as seen emerging at  $B \sim 350$  mT and  $f_q \sim 3.4$  GHz in Fig. 4(a), can be explained by a fluctuating parity of the Andreev states [4,5,8]. For instance, in the even-parity state, additional transition frequencies might be observed due to the hybridization of the qubit and Andreev-state transitions. However, in the odd-parity state (or vice versa [23,44]), only a single-qubit resonance might be observed, as the Andreev-state transitions no longer hybridize with the qubit mode. The observed spectrum is then the average of these different configurations, with parity switching occurring faster than the measurement time (typically  $> 10$  s for each vertical trace).

To further probe the spectrum, we sweep  $V_{\text{cut}}$  at fixed  $B$  [see Fig. 4(b)]. Here, the qubit transition is weakly dispersing around  $f_q \sim 3.4$  GHz. Two strongly gate-dependent

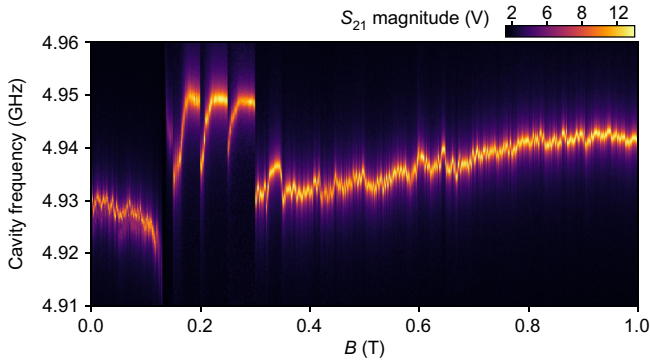


FIG. 5. The transmission voltage,  $S_{21}$ , as a function of the cavity drive frequency and  $B$  showing the field modulation of the resonance frequency of the  $\lambda/2$  cavity used for readout in Fig. 2. Due to the large fluctuations, the readout frequency is adjusted each time the magnetic field is varied. The large jumps around  $B = 0.2$  T are due to corrections of the out-of-plane magnetic field approximately 0.1 mT (not shown). At  $B \sim 150$  mT, the avoided crossing between the resonator and the second qubit is observed.

transitions oscillate around  $f_d \sim 3$  GHz, with both transitions giving rise to avoided crossings with the qubit transition. In addition, a second weakly gate-dependent state at  $f_d \sim 2.5$  GHz exhibits avoided crossings with the two oscillating transitions. The strong dispersion of the transitions with  $V_{\text{cut}}$  is consistent with Andreev states that are localized in the junction and therefore expected to be strongly dependent on the electrostatics of the junction.

The observation of anomalous qubit-resonance splittings has also been reported in Ref. [18]. This has been attributed to Andreev transitions emerging from phase winding associated with the reentrant lobe spectrum of the Little-Parks effect. The low-energy modes observed in this work may also emerge from phase winding effects, possibly explained by a proximitized surface charge layer that results in a Little-Parks-like spectrum. In both cases, the low-energy modes are very responsive to changes in the junction gate voltage. In this work, however, due to the tunability of the leads, the reentrant qubit spectrum is only observable for certain gate-voltage ranges and the specific charge distribution in the leads may also affect the phase dependence of the qubit-resonance splittings. It is noted that the period of the reentrant oscillations is smaller in Ref. [18] due to the use of larger-diameter nanowires, but in both cases the period is consistent with an integer number of flux quanta threading the nanowire.

#### V. CONCLUSIONS

We present a magnetic-field-resilient gatemon circuit with excellent relaxation times of  $5 \mu\text{s}$  at moderate magnetic fields, approximately 50 mT. The qubit retains coherence up to magnetic fields of 1 T with a lifetime  $T_1 \sim 0.6 \mu\text{s}$ , demonstrating the compatibility of our gatemon circuit design with magnetic fields typically needed for Majorana zero modes. Future work could integrate additional gates to allow greater control of the charge-carrier distribution along the nanowire or use a superconducting quantum interference device (SQUID)-like geometry to allow control of the superconducting phase across the Josephson junction. The combination of the microwave spectroscopy techniques with dc-transport measurements [45] may also provide further insights into the underlying origin of the observed features.

#### ACKNOWLEDGMENTS

We thank Arno Bargerbos, Bernard van Heck, Angela Kou, Leo Kouwenhoven, and Gijs de Lange for valuable discussions. This research was supported by Microsoft, the Danish National Research Foundation, and the European Research Council under Grant HEMs-DAM No. 716655.

## APPENDIX A: READOUT FREQUENCY CORRECTIONS

When applying an in-plane magnetic field,  $B$ , the readout resonator frequency,  $f_r$ , is modulated due to changes in the kinetic inductance of the Nb-Ti-N film. We therefore correct the readout frequency before each two-tone spectroscopy measurement by measuring the transmission voltage,  $S_{21}$ , as a function of the frequency with a vector-network analyzer (VNA) (see Fig. 5). Following each measurement, we fit  $S_{21}$  to a skewed Lorentzian to determine the readout frequency. These measurements are interleaved with the two-tone spectroscopy measurements shown in Fig. 2. We observe a slight degradation in  $f_r$  until the avoided crossing with the second qubit at  $B \sim 150$  mT is observed. The large jumps in  $f_r$  around  $B \sim 200$  mT are due to corrections to the out-of-plane field components carried out in between measurements, after observing a

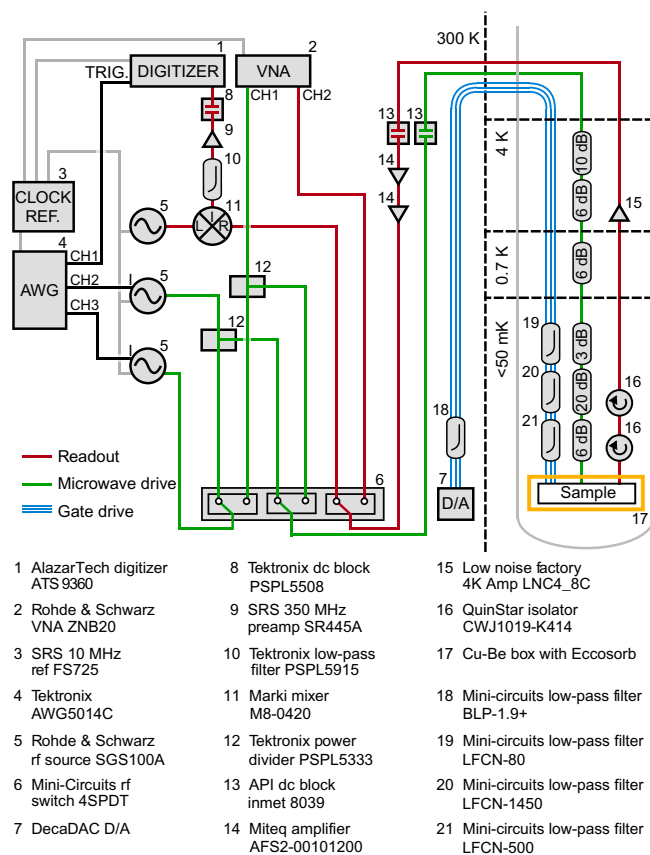


FIG. 6. A schematic of the experimental setup for the experiments presented. The readout resonator is driven either by the VNA or an arbitrary waveform generator (AWG)-modulated rf source (green lines). The output signal (red lines) is amplified and read out either with the VNA or down-converted by mixing with a reference signal. All microwave equipment is synchronized with a 10-MHz clock reference. Three dc lines (blue) are connected to the three gates,  $V_{\text{plg}}$ ,  $V_{\text{rplg}}$ , and  $V_{\text{cut}}$ , to tune the nanowire chemical potential and junction, respectively.

steady decrease in  $f_r$  when sweeping down from  $B = 1$  T. No significant degradation in the peak width is observed, highlighting the magnetic field compatibility of the readout resonators.

## APPENDIX B: EXPERIMENTAL SETUP

Figure 6 shows the experimental setup used for the measurements presented in the paper. The readout resonance frequency is determined by transmission measurements with a VNA. Two-tone spectroscopy and time-domain measurements are acquired with a heterodyne demodulation readout circuit. With this circuit, we measure the transmission of a pulse-modulated rf signal. We amplify the transmitted signal at 4 K and further at room temperature and then mix down with a reference signal before sampling and digital down-conversion. The demodulation circuit and VNA are connected to an rf switch matrix to allow switching between the two measurement configurations. The experiments are carried out in a dilution refrigerator with a 6-1-1 T vector magnet.

- [1] G. de Lange, B. van Heck, A. Bruno, D. J. van Woerkom, A. Geresdi, S. R. Plissard, E. P. A. M. Bakkers, A. R. Akhmerov, and L. DiCarlo, Realization of Microwave Quantum Circuits Using Hybrid Superconducting-Semiconducting Nanowire Josephson Elements, *Phys. Rev. Lett.* **115**, 127002 (2015).
- [2] T. W. Larsen, K. D. Petersson, F. Kueemeth, T. S. Jespersen, P. Krogstrup, J. Nygård, and C. M. Marcus, Semiconductor-Nanowire-Based Superconducting Qubit, *Phys. Rev. Lett.* **115**, 127001 (2015).
- [3] L. Casparis, N. J. Pearson, A. Kringhøj, T. W. Larsen, F. Kueemeth, J. Nygård, P. Krogstrup, K. D. Petersson, and C. M. Marcus, Voltage-controlled superconducting quantum bus, *Phys. Rev. B* **99**, 085434 (2019).
- [4] C. Janvier, L. Tosi, L. Bretheau, Ç. Ö. Girit, M. Stern, P. Bertet, P. Joyez, D. Vion, D. Esteve, M. F. Goffman, H. Pothier, and C. Urbina, Coherent manipulation of Andreev states in superconducting atomic contacts, *Science* **349**, 1199 (2015).
- [5] M. Hays, G. de Lange, K. Serniak, D. J. van Woerkom, D. Bouman, P. Krogstrup, J. Nygård, A. Geresdi, and M. H. Devoret, Direct Microwave Measurement of Andreev-Bound-State Dynamics in a Semiconductor-Nanowire Josephson Junction, *Phys. Rev. Lett.* **121**, 047001 (2018).
- [6] Y.-J. Doh, J. A. van Dam, A. L. Roest, E. P. A. M. Bakkers, L. P. Kouwenhoven, and S. De Franceschi, Tunable supercurrent through semiconductor nanowires, *Science* **309**, 272 (2005).
- [7] M. F. Goffman, C. Urbina, H. Pothier, J. Nygård, C. M. Marcus, and P. Krogstrup, Conduction channels of an InAs-Al nanowire Josephson weak link, *New J. Phys.* **19**, 092002 (2017).
- [8] D. J. van Woerkom, A. Proutski, B. van Heck, D. Bouman, J. I. Väyrynen, L. I. Glazman, P. Krogstrup, J. Nygård, L. P. Kouwenhoven, and A. Geresdi, Microwave spectroscopy

- of spinful Andreev bound states in ballistic semiconductor Josephson junctions, *Nat. Phys.* **13**, 876 (2017).
- [9] E. M. Spanton, M. Deng, S. Vaitiekėnas, P. Krogstrup, J. Nygård, C. M. Marcus, and K. A. Moler, Current-phase relations of few-mode InAs nanowire Josephson junctions, *Nat. Phys.* **13**, 1177 (2017).
- [10] A. Kringhøj, L. Casparis, M. Hell, T. W. Larsen, F. Kuemmeth, M. Leijnse, K. Flensberg, P. Krogstrup, J. Nygård, K. D. Petersson, and C. M. Marcus, Anharmonicity of a superconducting qubit with a few-mode Josephson junction, *Phys. Rev. B* **97**, 060508(R) (2018).
- [11] A. Bargerbos, W. Uilhoorn, C.-K. Yang, P. Krogstrup, L. P. Kouwenhoven, G. de Lange, B. van Heck, and A. Kou, Observation of Vanishing Charge Dispersion of a Nearly Open Superconducting Island, *Phys. Rev. Lett.* **124**, 246802 (2020).
- [12] A. Kringhøj, B. van Heck, T. W. Larsen, O. Erlandsson, D. Sabonis, P. Krogstrup, L. Casparis, K. D. Petersson, and C. M. Marcus, Suppressed Charge Dispersion via Resonant Tunneling in a Single-Channel Transmon, *Phys. Rev. Lett.* **124**, 246803 (2020).
- [13] V. Mourik, K. Zuo, S. M. Frolov, S. R. Plissard, E. P. A. M. Bakkers, and L. P. Kouwenhoven, Signatures of Majorana fermions in hybrid superconductor-semiconductor nanowire devices, *Science* **336**, 1003 (2012).
- [14] S. M. Albrecht, A. P. Higginbotham, M. Madsen, F. Kuemmeth, T. S. Jespersen, J. Nygård, P. Krogstrup, and C. M. Marcus, Exponential protection of zero modes in Majorana islands, *Nature* **531**, 206 (2016).
- [15] R. M. Lutchyn, E. P. A. M. Bakkers, L. P. Kouwenhoven, P. Krogstrup, C. M. Marcus, and Y. Oreg, Majorana zero modes in superconductor-semiconductor heterostructures, *Nat. Rev. Mater.* **3**, 52 (2018).
- [16] F. Luthi, T. Stavenga, O. W. Enzing, A. Bruno, C. Dickel, N. K. Langford, M. A. Rol, T. S. Jespersen, J. Nygård, P. Krogstrup, and L. DiCarlo, Evolution of Nanowire Transmon Qubits and Their Coherence in a Magnetic Field, *Phys. Rev. Lett.* **120**, 100502 (2018).
- [17] D. Sabonis, O. Erlandsson, A. Kringhøj, B. van Heck, T. W. Larsen, I. Petkovic, P. Krogstrup, K. D. Petersson, and C. M. Marcus, Destructive Little-Parks Effect in a Full-Shell Nanowire-Based Transmon, *Phys. Rev. Lett.* **125**, 156804 (2020).
- [18] A. Kringhøj, G. W. Winkler, T. W. Larsen, D. Sabonis, O. Erlandsson, P. Krogstrup, B. van Heck, K. D. Petersson, and C. M. Marcus, Andreev Modes from Phase Winding in a Full-Shell Nanowire-Based Transmon, *Phys. Rev. Lett.* **126**, 047701 (2021).
- [19] M. Pita-Vidal, A. Bargerbos, C.-K. Yang, D. J. van Woerkom, W. Pfaff, N. Haider, P. Krogstrup, L. P. Kouwenhoven, G. de Lange, and A. Kou, Gate-Tunable Field-Compatible Fluxonium, *Phys. Rev. Appl.* **14**, 064038 (2020).
- [20] J. Kroll, W. Uilhoorn, K. van der Enden, D. de Jong, K. Watanabe, T. Taniguchi, S. Goswami, M. Cassidy, and L. Kouwenhoven, Magnetic field compatible circuit quantum electrodynamics with graphene Josephson junctions, *Nat. Commun.* **9**, 4615 (2018).
- [21] E. Ginossar and E. Grosfeld, Microwave transitions as a signature of coherent parity mixing effects in the Majorana-transmon qubit, *Nat. Commun.* **5**, 4772 (2014).
- [22] K. Yavilberg, E. Ginossar, and E. Grosfeld, Fermion parity measurement and control in Majorana circuit quantum electrodynamics, *Phys. Rev. B* **92**, 075143 (2015).
- [23] L. Tosi, C. Metzger, M. F. Goffman, C. Urbina, H. Pothier, S. Park, A. L. Yeyati, J. Nygård, and P. Krogstrup, Spin-Orbit Splitting of Andreev States Revealed by Microwave Spectroscopy, *Phys. Rev. X* **9**, 011010 (2019).
- [24] A. Imamoglu, Cavity QED Based on Collective Magnetic Dipole Coupling: Spin Ensembles as Hybrid Two-Level Systems, *Phys. Rev. Lett.* **102**, 083602 (2009).
- [25] V. Ranjan, G. de Lange, R. Schutjens, T. Debelhoir, J. P. Groen, D. Szombati, D. J. Thoen, T. M. Klapwijk, R. Hanson, and L. DiCarlo, Probing Dynamics of an Electron-Spin Ensemble via a Superconducting Resonator, *Phys. Rev. Lett.* **110**, 067004 (2013).
- [26] W. D. Oliver and P. B. Welander, Materials in superconducting quantum bits, *MRS Bull.* **38**, 816 (2013).
- [27] P. Kumar, S. Sendelbach, M. A. Beck, J. W. Freeland, Z. Wang, H. Wang, C. C. Yu, R. Q. Wu, D. P. Pappas, and R. McDermott, Origin and Reduction of  $1/f$  Magnetic Flux Noise in Superconducting Devices, *Phys. Rev. Appl.* **6**, 041001(R) (2016).
- [28] J. G. Kroll, F. Borsoi, K. L. van der Enden, W. Uilhoorn, D. de Jong, M. Quintero-Pérez, D. J. van Woerkom, A. Bruno, S. R. Plissard, D. Car, E. P. A. M. Bakkers, M. C. Cassidy, and L. P. Kouwenhoven, Magnetic-Field-Resilient Superconducting Coplanar-Waveguide Resonators for Hybrid Circuit Quantum Electrodynamics Experiments, *Phys. Rev. Appl.* **11**, 064053 (2019).
- [29] We find that the use of aluminum on-chip bond wire crossovers to connect ground planes causes a large amount of dissipation above the critical field of aluminum.
- [30] P. Krogstrup, N. L. B. Ziino, W. Chang, S. M. Albrecht, M. H. Madsen, E. Johnson, J. Nygård, C. M. Marcus, and T. S. Jespersen, Epitaxy of semiconductor-superconductor nanowires, *Nat. Mater.* **14**, 400 (2015).
- [31] Electrodes spaced approximately  $1\ \mu\text{m}$  apart on bare high-resistivity silicon will leak at approximately  $\pm 10\ \text{V}$  at base temperature.
- [32] COMSOL, Inc. (<http://www.comsol.com>).
- [33] X. Mi, J. V. Cady, D. M. Zajac, J. Stehlik, L. F. Edge, and J. R. Petta, Circuit quantum electrodynamics architecture for gate-defined quantum dots in silicon, *Appl. Phys. Lett.* **110**, 043502 (2017).
- [34] Ö. Gül, H. Y. Günel, H. Lüth, T. Rieger, T. Wenz, F. Haas, M. Lepsa, G. Panaitov, D. Grützmacher, and T. Schäpers, Giant magnetoconductance oscillations in hybrid superconductor-semiconductor core/shell nanowire devices, *Nano Lett.* **14**, 6269 (2014).
- [35] G. W. Winkler, A. E. Antipov, B. van Heck, A. A. Soluyanov, L. I. Glazman, M. Wimmer, and R. M. Lutchyn, Unified numerical approach to topological semiconductor-superconductor heterostructures, *Phys. Rev. B* **99**, 245408 (2019).
- [36] A. E. Antipov, A. Bargerbos, G. W. Winkler, B. Bauer, E. Rossi, and R. M. Lutchyn, Effects of Gate-Induced Electric

- Fields on Semiconductor Majorana Nanowires, [Phys. Rev. X \*\*8\*\*, 031041 \(2018\)](#).
- [37] K. Zuo, V. Mourik, D. B. Szombati, B. Nijholt, D. J. van Woerkom, A. Geresdi, J. Chen, V. P. Ostroukh, A. R. Akhmerov, S. R. Plissard, D. Car, E. P. A. M. Bakkers, D. I. Pikulin, L. P. Kouwenhoven, and S. M. Frolov, Supercurrent Interference in Few-Mode Nanowire Josephson Junctions, [Phys. Rev. Lett. \*\*119\*\*, 187704 \(2017\)](#).
- [38] A. Danilenko, *et al.*, To be published.
- [39] N. Kosugi, S. Matsuo, K. Konno, and N. Hatakenaka, Theory of damped Rabi oscillations, [Phys. Rev. B \*\*72\*\*, 172509 \(2005\)](#).
- [40] G. Ithier, E. Collin, P. Joyez, P. J. Meeson, D. Vion, D. Esteve, F. Chiarello, A. Shnirman, Y. Makhlin, J. Schrieffer, and G. Schön, Decoherence in a superconducting quantum bit circuit, [Phys. Rev. B \*\*72\*\*, 134519 \(2005\)](#).
- [41] G. Catelani, R. J. Schoelkopf, M. H. Devoret, and L. I. Glazman, Relaxation and frequency shifts induced by quasiparticles in superconducting qubits, [Phys. Rev. B \*\*84\*\*, 064517 \(2011\)](#).
- [42] W. Uilhoorn, *et al.*, To be published.
- [43] A. Keselman, C. Murthy, B. van Heck, and B. Bauer, Spectral response of Josephson junctions with low-energy quasiparticles, [SciPost Phys. \*\*7\*\*, 50 \(2019\)](#).
- [44] M. Hays, V. Fatemi, K. Serniak, D. Bouman, S. Diamond, G. de Lange, P. Krogstrup, J. Nygård, A. Geresdi, and M. H. Devoret, Continuous monitoring of a trapped superconducting spin, [Nat. Phys. \*\*16\*\*, 1103 \(2020\)](#).
- [45] A. Kringhøj, T. W. Larsen, B. van Heck, D. Sabonis, O. Erlandsson, I. Petkovic, D. I. Pikulin, P. Krogstrup, K. D. Petersson, and C. M. Marcus, Controlled dc Monitoring of a Superconducting Qubit, [Phys. Rev. Lett. \*\*124\*\*, 056801 \(2020\)](#).